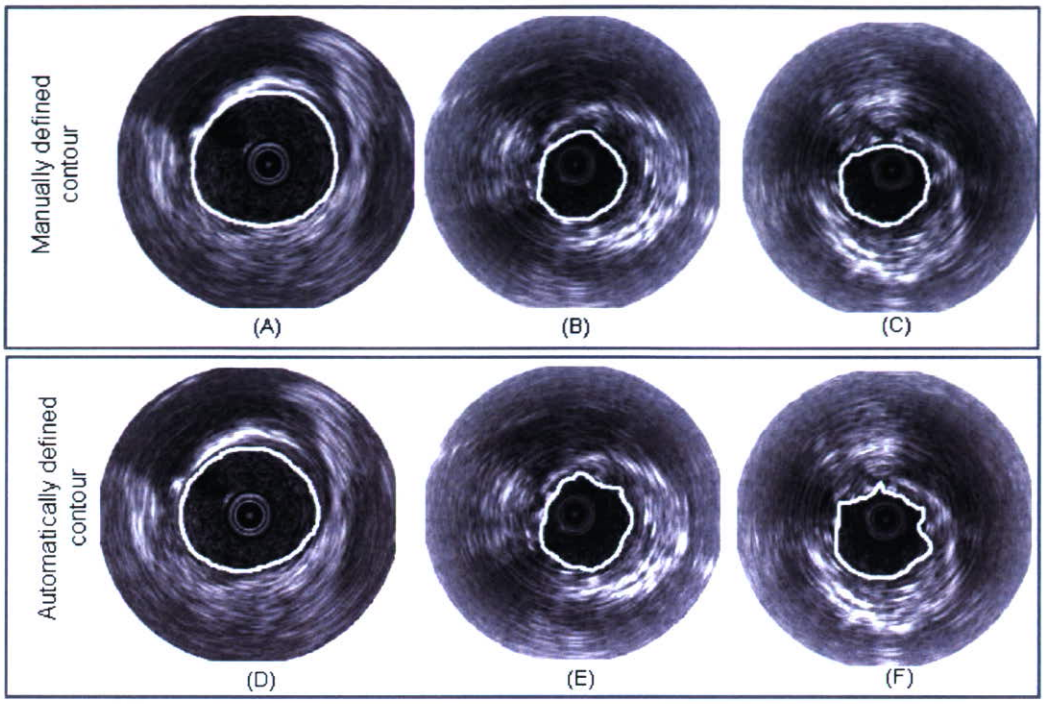

Fig. 8. Comparison between images automatically segmented and gold standard segmented images

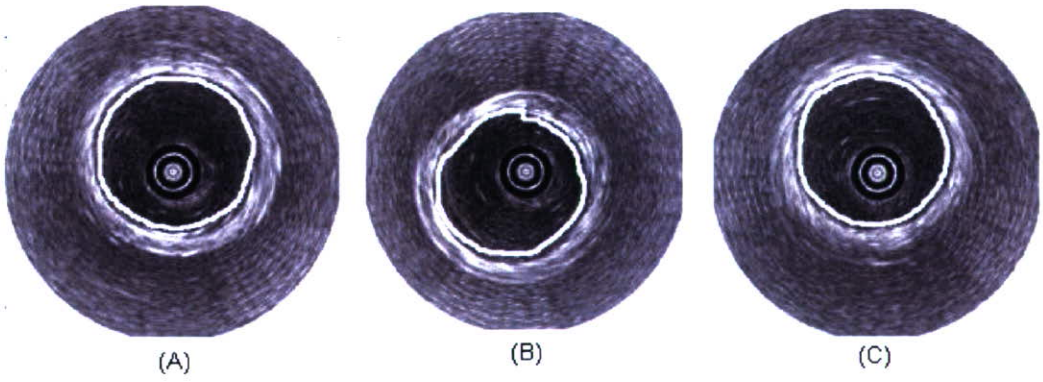

Fig. 9. Examples of automatically segmented images obtained from phantoms

Parametric Intravascular Ultrasound Imaging

Two-dimensional Tissue Velocity Imaging and Self-organizing Map Imaging

Y. Saijo, E. Santos Filho, T. Yambe
Department of Medical Engineering and Cardiology
Institute of Development, Aging and Cancer, Tohoku University
4-1 Seiryomachi, Aoba-ku, Sendai 980-8575, Japan
saijo@idac.tohoku.ac.jp

A. Tanaka
Faculty of Symbiotic Systems Science
Fukushima University
1 Kanayagawa, Fukushima 960-1296, Japan

T. Iwamoto, M. Yoshizawa
Graduate School of Engineering
Tohoku University
6-6-05 Aramaki-aza-Aoba, Aoba-ku, Sendai 980-8579, Japan

Y. Akino, Y. Hanadate
Department of Cardiology
Miyagi Social Insurance Hospital
143 Nakadamachi-aza-Maeoki, Taihaku-ku, Sendai 981-1103, Japan

Abstract— **We have been developing some methods for quantitative analysis of intravascular ultrasound (IVUS) imaging. In this paper, we present two-dimensional (2D) intravascular tissue velocity imaging and self-organizing map imaging. RF signal of 40-MHz IVUS apparatus was obtained by an A/D converter with sampling rate of 500-MSa-s. IVUS images were reconstructed from RF data sets and the images were divided into square shaped regions of interest (ROIs). The correlation and displacement of the ROIs between the consecutive two frames were calculated by template-matching method. Two-dimensional tissue velocity was defined as the vectors of displacement of ROI with 0.7 and more correlation. For self-organizing map (SOM) imaging, the frequency spectrum was calculated for each position of the hamming window using a mathematical autoregressive (AR) model. The optimized AR spectra were used to compute 18 spectral shape parameters for each ROI to construct SOM. Spectra were automatically classified into seven categories which may corresponded with catheter, guidewire shadow, blood, fibrosis, calcification, lipid, media and others.**

Keywords; intravascular ultrasound, tissue velocity imaging, self organizing map, coronary artery, atherosclerosis

I. INTRODUCTION

Intravascular ultrasound (IVUS) has been clinically applied since early 1990's and it has become an important clinical tool for investigation of coronary artery during percutaneous transluminal coronary intervention (PCI) therapies. IVUS is mainly used to measure the luminal and vascular areas and to confirm the full expansion of the coronary stent to the arterial wall. Besides the measurement of dimensions, IVUS also provides important information on tissue character of atherosclerosis.

First objective of the present study is to develop an algorithm for two-dimensional tissue velocity vector and strain of coronary artery. Second objective is to develop self-organizing map (SOM) imaging based on spectral analysis of radiofrequency (RF) signal for automatic plaque classification.

II. METHODS

A. RF Data Acqisuition

A commercial available IVUS system (Clear View Ultra, Boston Scientific, USA) was equipped. The central frequency of the IVUS probe (Atlantis SR Pro, Boston Scientific, USA) was 40 MHz and the pulse repetition rate was 7680 Hz. A single frame of the IVUS system consisted of 256 lines so that 7680 pulses made 30 f/s. An analogue to digital (A/D)

converter board (CompuScope 8500, Gage, USA) was connected to the RF output of the IVUS apparatus. The sampling rate was 500 MSa/s, the resolution was 8-bit and the on-board memory was 8 MB. Intra-coronary pressure was measured by fluid-filled method using 6 French (approximately 2.0 mm) diameter guiding catheter which was inserted into coronary artery. Biological signals such as electrocardiogram and intra-coronary pressure were simultaneously recorded using an A/D converter (PCI-6024E, National Instruments, USA) with the sampling rate of 100 kSa/s and the resolution of 12-bit [1].

After the RF data were sent to the workstation, the signals were pre-treated for further analyses. As the original RF signal consisted of one line, the data was divided into 10 matrixes. Each matrix consisted of 3053 lines by 256 columns and processed for one frame of IVUS image.

B. 2D Tissue Velocity Imaging

First, 30 to 50 MHz component of the original RF signal was extracted by using a software-based bandpass filtering method. Second, the original signal consisting of one line was divided into 10 matrixes. Each matrix consisted of 3053 lines by 256 columns and processed for one frame of IVUS image.

Ideally, one frame consisting of 256 lines of the rotational IVUS is equivalent to that of phased-array IVUS. However, a conventional rotating IVUS system uses frame trigger to adjust frame to frame rotational dis-uniformity. This indicates the position of the 'n/256'th line is not guaranteed to be at the same position of the previous frame. Then the correlation coefficient between two consecutive matrixes was calculated in the rotational direction and the rotational dis-uniformity was corrected in rotational direction to obtain the maximum correlation coefficient.

Conventional IVUS image was generated by converting polar coordinate of original RF signal matrix to rectangular coordinate. Then the IVUS image was divided into 64 by 64 square shaped regions of interest (ROIs). Pattern matching method was applied for calculation of correlation and displacement of the ROIs between the consecutive two frames.

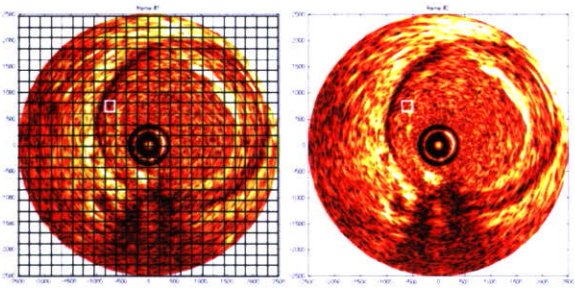

Figure 1. Re-construced IVUS images and segmentation

Figure 1 shows the reconstructed IVUS image (left) divided into 64 by 64 square shaped regions of interest. If the position of the center of the ROI (white highlighted square in the left image) is $p\ (x_0, y_0)$ and the center of matched ROI (white highlighted square in the right image) is in the next frame is $q\ (x_1, y_1)$, the displacement vector v is defined as

$$\vec{v} = (x_1 - x_0, y_1 - y_0) \cdots (1)$$

Two-dimensional tissue velocity was defined as the vectors of displacement divided by 33 ms (interval of two consecutive frames). The correlation between the two frames was high when the tissues were remained nearly same positions during 33 ms. We assumed that the ROI with 0.7 and more correlation coefficient was vascular wall. Tissue velocity vectors with the correlation more than 0.7 were overlaid on the conventional IVUS image. Figure 2 shows the correlation (left) and 2D tissue velocity imaging.

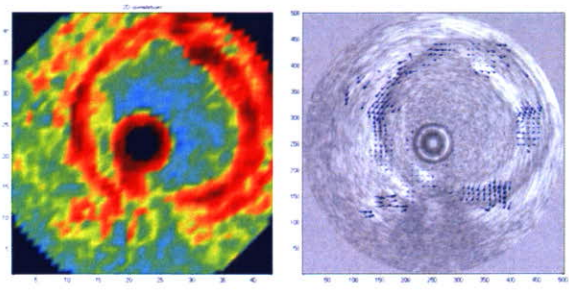

Figure 2. Correlation (left) and 2D tissue velocity imaging (right)

Tissue strain was defined as the change of the ROI area between two frames.

C. Self-organizing Map

1) Pre-treatment of the data

IVUS data were acquired with a commercially available IVUS system with the central frequency of 40MHz. RF data were digitized and stored in a workstation using by an A/D board with the sampling frequency of 500Msa/s and the resolution of 8 bits. Initially, a software-based band-pass filter (15MHz-105MHz) was applied to the IVUS RF signal data. Then each line in the ROI was scanned by a 128-points width hamming window. The frequency spectrum was calculated for each position of the hamming window using fast Fourier transform (FFT) and a mathematical autoregressive (AR) model. Akaike's final prediction error method estimated the optimum AR model order was 15 for characterizing plaque components. Figure 3 shows the raw RF signal wavelet consisted of 128 points. Figure 4 is the FFT and Figure 5 is the AR model.

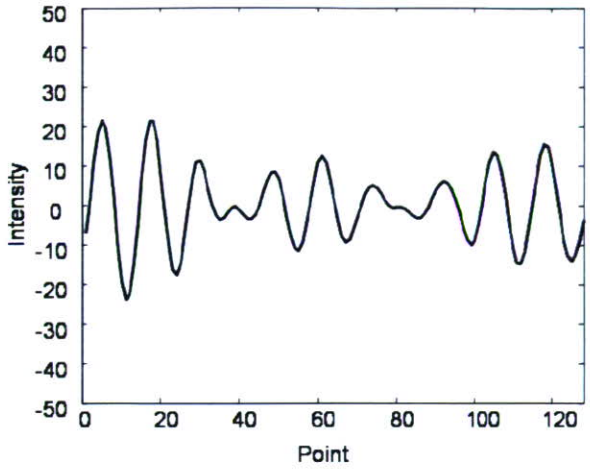

Figure 3. Raw RF data with 128 points

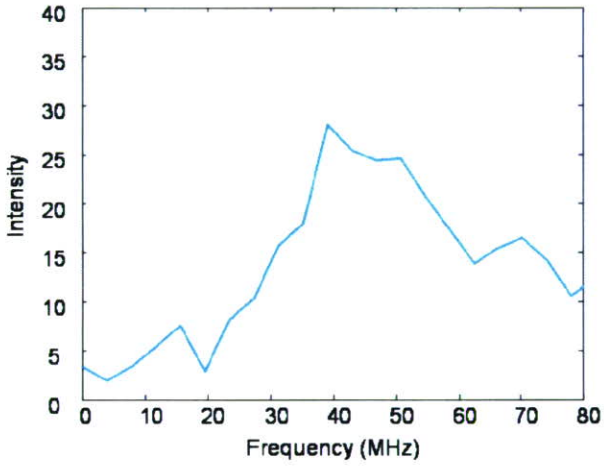

Figure 4. Spectrum calculated by FFT

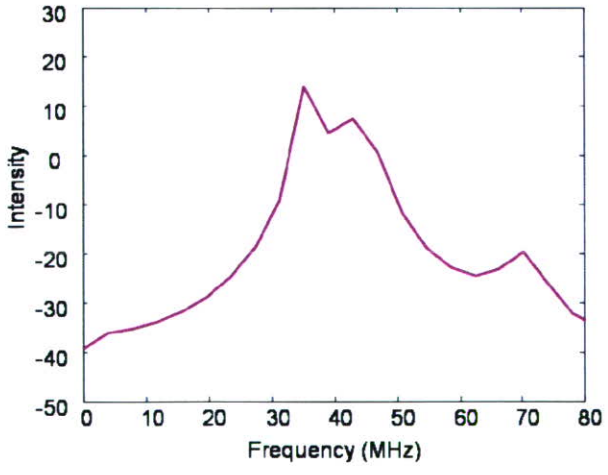

Figure 5. Spectrum calculated by AR method

Further, the optimized AR spectra were used to compute 18 spectral shape parameters for each ROI. These parameters were: 1. power and 2. frequency of fundamental wave, 3. power and 4. frequency of second harmonic wave, 5. local minimum power between fundamental wave power and second harmonic wave power, 6. frequency of local minimum power, 7. maximum power, 8. frequency of maximum power, 9. slope from power at frequency 15MHz to fundamental wave power, 10. corresponding y-intercept, 11. slope from fundamental wave power to local minimum power, 12. corresponding y-intercept, 13. slope from local minimum power to second harmonics power, 14. corresponding y-intercept, 15. slope from second harmonics power to 100MHz power, 16. corresponding y-intercept, 17. mean of integrated backscatter, and 18. ROI position at line.

2) SOM

The SOM is one of neural network application and it is a vector quantization method that places the weight vectors on a regular low-dimensional grid in an ordered fashion. A SOM consists of neurons organized on a regular grid. Each neuron is a *d*-dimensional weight vector where *d* is equal to the dimension of the input data vectors. The neurons are connected to adjacent neurons by a neighborhood relation, which dictates the topology, or structure, of the map.

In this study, the SOM classifier learned the spectral parameters for training. And then the SOM classifier classified windowed area of IVUS data based on these parameters. Finally, the tissue maps were reconstructed on IVUS B-mode images based on the SOM.

III. RESULTS

Figure 6 shows an example of color-coded IVUS image, correlation, 2D tissue velocity, 2D tissue strain and corresponded coronary tissue obtained by directional coronary atherectomy (DCA).

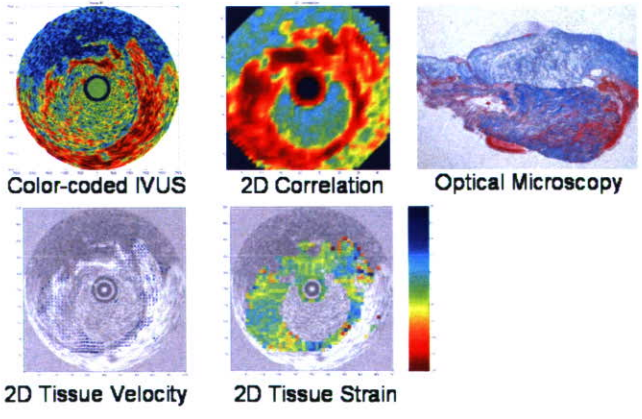

Figure 6. Color-coded IVUS image, correlation, 2D tissue velocity, 2D tissue strain and corresponded coronary tissue obtained by DCA

2D tissue velocity and strain are heterogeneous in this lesion and the optical microscopy shows the collagen-rich

fibrosis, smooth muscle, necrotic core and thrombus. The inhomogeneity of the sample is well represented by 2D tissue velocity and strain imaging.

Figure 7 is the SOM of the training data sets. Eighteen spectral parameters consisted 18-dimensional data were represented on a 2-dimensional map. In this way, the SOM classified the RF spectrum into seven categories. Figure 8 is the conventional IVUS image (left) and color-coded image based on automatic classification by SOM (right).

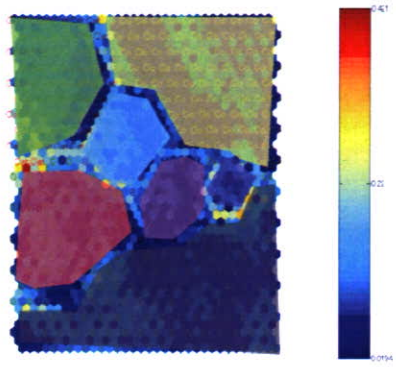

Figure 7. SOM classified the RF spectra into seven categories. 18-dimensional parameters were displayed on a 2-dimensional map.

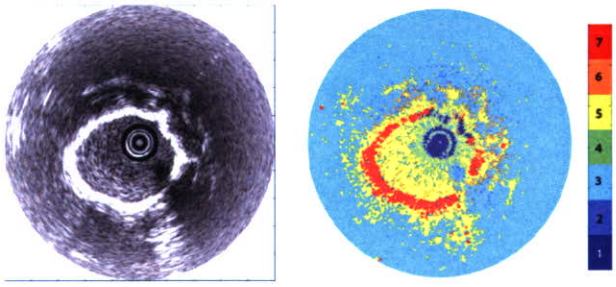

Figure 8. Conventional IVUS image (left) and color-coded image based on automatic classification by SOM (right)

IV. Discussion

The group at Erasmus University lead by van der Steen and de Korte has been applying correlation analysis technique to obtain vascular elasticity information using phased array IVUS system [2-4] because RF-line pairs between two consecutive frames are always guaranteed as coming from the same position of the tissue. Correlation analysis using rotating IVUS has been considered as difficult but the present study showed that correlation image clearly identified the vascular wall of coronary artery. The two-dimensional tissue velocity and strain derived by the method provide important information on tissue character. A vulnerable plaque showed heterogeneous strain indicating the tissue components are also inhomogeneous.

Virtual histology® (VH) has been clinically applied technique to classify coronary plaque into four categories. The technique is also based on RF spectral analysis. By our SOM analysis, the spectra were classified into seven categories which may corresponded with catheter, guidewire shadow, blood, fibrosis, calcification, lipid, media and others. Integration of these two techniques and introduction of the micro acoustic properties measured by acoustic microscopy may develop the algorithm.

V. Conclusions

We have developed two novel image analysis algorithms for IVUS. 2D tissue strain imaging corresponded well to the DCA-excised histological specimen. SOM analysis automatically classified the RF spectra of the IVUS image and it may provide additional information of the tissue character besides conventional gray-scale imaging to cardiologists.

Acknowledgments

This study was supported by Grants-in-Aid for Scientific Research (Scientific Research (B) 15300178, Scientific Research (B) 15360217) from the Japan Society for the Promotion of Science and Health and Labor Sciences Research Grants from the Ministry of Health, Labor and Welfare for the Research on Advanced Medical Technology (H17-Nano-001).

References

[1] Y. Saijo, A. Tanaka, N. Owada, Y. Akino, S. Nitta. Tissue velocity imaging of coronary artery by rotating-type intravascular ultrasound. Ultrasonics. 42(2004), pp. 753-757.

[2] A.F. van der Steen, C.L. de Korte, E.I. Cespedes. Intravascular ultrasound elastography. Ultraschall Med. 19(1998), pp.196-201.

[3] C.L. de Korte, G. Pasterkamp, A.F. van der Steen, H.A. Woutman, N. Bom. Characterization of plaque components with intravascular ultrasound elastography in human femoral and coronary arteries in vitro. Circulation 102 (2000), pp. 617-623.

[4] C.L. de Korte, M.J. Sierevogel, F. Mastik, C. Strijder, J.A. Schaar, E. Velema, G. Pasterkamp, P.W. Serruys, A.F. van der Steen. Identification of atherosclerotic plaque components with intravascular ultrasound elastography in vivo: a Yucatan pig study. Circulation 105 (2002), pp.1627-30.

Automatic Luminal Contour and Calcification Detection in Intravascular Ultrasound Images

Esmeraldo dos Santos Filho[1], Yoshifumi Saijo[2], Makoto Yoshizawa[3] and Akira Tanaka[4]
1 Graduate School of Engineering, Tohoku University
2 Institute of Development, Aging and Cancer, Tohoku University
3 Information Synergy Center, Tohoku University
4 College of Symbiotic Systems Science, Fukushima University
esmeraldo@ieee.org

***Abstract*—Innovative applications of image processing techniques for analysis of intravascular ultrasound images are presented. This work has two main objectives: (1) to detect the luminal contour which is necessary to assess the degree of vessel stenosis, and (2) to detect presence of calcification, which is an important information for definition of the intervention method. These problems were addressed using a combination of mathematical morphology techniques, fuzzy systems, and *a priori* knowledge of the problems. Encouraging results were found when the results were compared with images manually segmented by expert medical doctors.**

Keywords: ultrasound; texture; image segmentation

I. INTRODUCTION

The objective of this work is to develop a system for automatic segmentation of calcifications and luminal contour in intravascular ultrasound (IVUS) images as a tool to support coronary artery disease diagnosis.

Luminal contour segmentation is important because the lumen area can give the medical doctor information about the degree of vessel stenosis. On the other hand, the presence or absence of calcium demonstrated by IVUS has been shown to be an important determinant of the transcatheter intervention success.

However, in general, autonomous segmentation is one of the most difficult tasks in digital image processing. Segmentation accuracy determines the eventual success or failure of computerized analysis procedures.

In this paper, as in Brusseau's [1] and Bovenkamp's [2] works, we proposed a system for automatic luminal contour segmentation. Unlike the Brusseau's system, our system is applied on images obtained from a rotating IVUS system due to the fact that these systems are largely used in clinical settings. Instead of a multi-agent system, as proposed by Bovenkamp, we used a simpler and powerful set of features proposed by Tuceryan [3] to achieve our goal of luminal contour segmentation.

Our strategy to achieve this goal is to extract local moment based texture features and a proposed pixel position feature from IVUS images to perform clustering on the basis of these features.

This work was supported by Health and Labor Sciences Research Grants H15-Fiji-001 of Ministry of Health Labor and Welfare of Japan and the Grant of Tohoku University 21 COE Program: 'Future Medical Engineering based on Bio-nanotechnology'.

II. MATERIALS AND METHODS

In this work, we used a commercial available IVUS system (Clear View Ultra, Boston Scientific, USA). The central frequency of the rotating IVUS probe (Atlantis SR Pro, Boston Scientific, USA) was 40 MHz..

A. Moments

Our algorithm uses the moments of an image to compute texture features. The $(p+q)$-th order moment m_{pq} of a function of two variables $f(x,y)$ with respect to the origin (0,0) is defined as [3]:

$$m_{pq} = \int_{-\infty}^{\infty} \int_{-\infty}^{\infty} f(x,y) x^p y^q dxdy \qquad (1)$$

where $p,q = 0,1,2, \ldots$

In this paper, as in Tuceryan's work [3], we regard the intensity image as a function of two variables, $f(x,y)$. We compute a fixed number of the lower order moments for each pixel in the input image (we use $p+q \leq 2$). The moments are computed within a small local window around each pixel. Given a window size W, the coordinates are normalized to the range of [-0.5 , 0.5] and the pixel is located at the center. The moments are computed with respect to this normalized coordinate system. This permits us to compare the set of moments computed for each pixel.

Let (i,j) be the pixel coordinates for which the moments are computed. For a pixel with coordinates (k,l) which falls within the window, the normalized coordinates (x_k, y_l) are given by:

$$x_k = \frac{k-i}{W} \qquad y_l = \frac{l-j}{W} \qquad (2)$$

Then the moment $m_{pq}(i,j)$ within a window centered at pixel (i,j) is computed by a discrete sum approximation of Equation (1) that uses the normalized coordinates:

$$m_{pq} = \sum_{k=-W/2}^{W/2} \sum_{l=-W/2}^{W/2} f(i+k, j+l) x_k^p y_l^q \qquad (3)$$

This discrete computation of the set of moments for a given pixel over a finite rectangular window corresponds to a neighborhood operation, and, therefore, it can be interpreted as a convolution of the image with a mask [3].

The set of values for each moment over the entire image can be regarded as a feature image. Let M_k be the *k*-th such image. If we use *n* moments, then there will be *n* such moment images. In our experiments, we used up to second order moments. That is, we used m_{00}, m_{01}, m_{10}, m_{11}, m_{02}, m_{20} which result in the images, M_1, M_2, M_3, M_4, M_5, and M_6 respectively.

To enhance the discrimination power of these moments, we adopted the transformation used by Tuceryan [3]. Then, we introduced a nonlinear transformation that maps moments to texture features.

Thus, we obtain the texture feature image F_k corresponding to the moment image M_k with mean $\overline{M_k}$ using the following transformation:

$$F_k(i,j) = \frac{1}{L^2} \sum_{(a,b)\in\omega_{ij}} \left| \tanh\left(\sigma\left(M_k(a,b) - \overline{M_k}\right)\right)\right| \quad (4)$$

where: ω_{ij} is an $L \times L$ averaging window centered at location (i,j) and σ controls the shape of the function. The parameters (in Eq.4): σ, moment window size *W*, and average window size *L* were chosen by gradually adjusting these values and observing the resultant effect in the segmented images. The final chosen values were W=7, L=9 and $\sigma = 0.01$. They were determined empirically.

B. Luminal Contour Definition

Due to the encouraging results obtained by Tuceryan [3], the theory of moment based texture segmentation was applied to the problem of luminal contour detection in IVUS images. The system proposed in this paper is comprised by the following modules.

Input image. The input image is the original image obtained from the IVUS system described in the beginning of this section.

Feature extraction. The feature extraction module is in charge of extraction of the transformed versions of the moments, F_k; k=1, 2, ...,6, and the radial distance *R* presented graphically in Fig.1.

In this work, we define the radial distance *R* as the distance from the central pixel of the image and the position of the pixel *P* under consideration. This distance *R* is normalized and becomes the seventh feature used in the following clustering of the input image pixels. The radial distance *R* is of fundamental importance because it helps pixels that are at similar distance from the center of the image to be included in the same cluster if they have similar texture features. The effect of using these texture and position features is that the clusters become organized in regions similar to concentric rings around the central pixel. This is associated with physiological structure of the blood vessels as represented in Fig.1. Thus, these seven features are used to comprise a feature vector for each pixel of the image.

Clustering. Based on their feature vectors, the input image pixels were clustered in this module using the Fuzzy C Means algorithm [4]. The chosen number of clusters was four: one cluster for the region outside the vessel, one for the region between the adventitia and intima, one for the lumen and another one for the catheter zone.

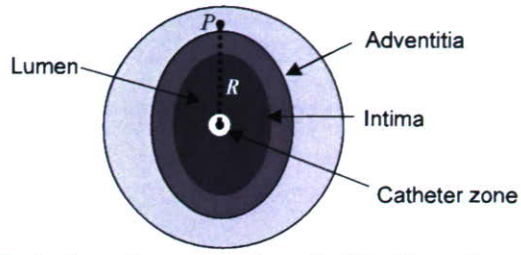

Fig.1 – Illustration of a cross section of a blood vessel

Morphological contour smoothing. In order to reduce the irregularities of the borders as well as some small regions around the borders, a morphological filtering is done prior to boundary detection. This filtering is performed through the application of opening and closing morphological operations with a disk structuring element of size 3.

Boundary detection. After the clustering and contour smoothing, the images had very well defined regions that could have their contour easily detected by traditional edge detection methods. In this system we used the Sobel operator due to its simplicity and efficiency.

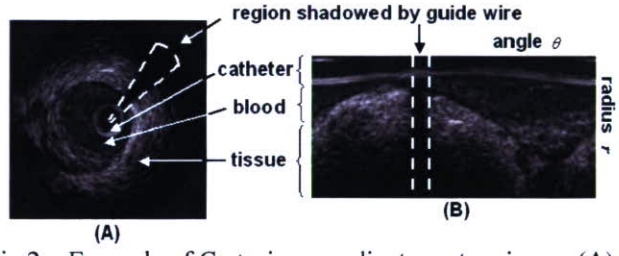

Fig.2 – Example of Cartesian coordinate system image (A) and its corresponding polar coordinate system version (B)

Output image. An example of the final output image can be observed in Fig.4(A).

C. The Guide Wire Shadow Problem

Sometimes due to the presence of the guide wire a region of the input image becomes shadowed and then contains no texture information. This may causes segmentation error. To solve this problem we proposed a contour correction procedure comprised of the following steps:

1) Convert the image with segmentation error from Cartesian coordinate system to polar coordinate system. An example of this process is shown in Fig.2.

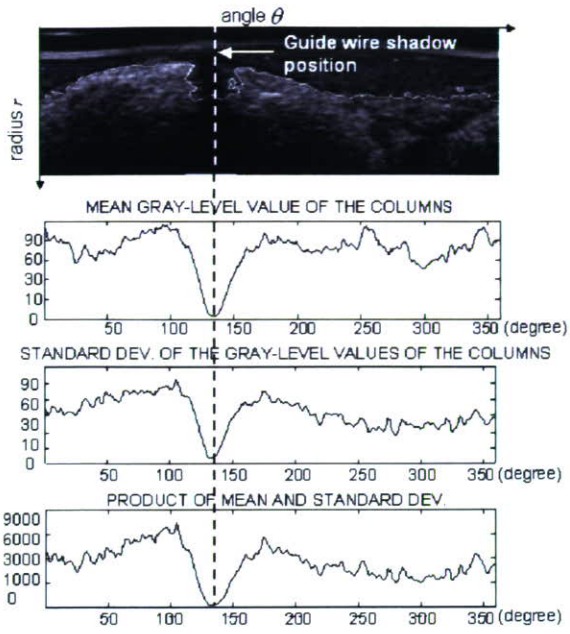

Fig.3 – Example of the search for the guide wire shadow position in polar coordinate system image based on the values of mean gray level and standard deviation of each column.

2) Automatically find the guide wire shadow. This step is carried out through the calculus of the mean gray-level and standard deviation of every column of the polar coordinate system converted image. The column which contains minimum value of the product of the mean gray-level by standard deviation is assumed to be the position of the guide wire shadowed region as illustrated in Fig.3. The catheter region was ignored during this process to avoid the influence of the ring-down artifact.

3) Erase the contour wrongly drawn in the guide wire shadow region and draw a new contour in the erased region through linear interpolation.

4) Convert the corrected image back to the Cartesian system.

RESULTS AND DISCUSSION I

Using the system presented above, tests were done with 15 *in vivo* coronary IVUS images from different patients. High correlation coefficients between the luminal contour automatically and the contour manually detected were found. These correlation coefficients values revealed preservation of standard deviation (0.92), mean gray level (0.89), and area (0.87) in the regions automatically segmented. An example of the results is shown in Fig.4 together with the image segmented by a medical doctor for comparison.

Our preliminary tests suggest that the moment based texture features together with the radial distance are feasible components for a feature vector in IVUS image segmentation when the aim is to find the luminal contour. A contour correction procedure based on the mean gray level and variance of each column of the polar coordinate version of the input image was presented as a feasible solution for the problem of error generated by the guide wire shadow.

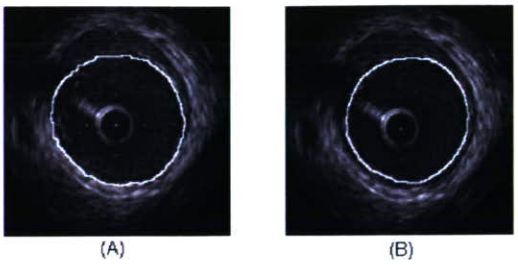

Fig.4 – Example of luminal contour detection. (A) and (B) are the same images obtained from patient A. (A) Automatically defined contour. (B) manually defined contour

IV CALCIFICATION DETECTION

One of the characteristics of the calcification regions is that they usually present high intensity echo for IVUS images. This fact makes it possible to segment calcified regions by gray level threshold techniques. However as the intensity level change from image to image it is quite difficult to find a single threshold level that could provide an accurate segmentation for a large group of images. Thus, it is necessary to adapt the threshold level to every single image.

A. Adaptive Threshold Estimator

Otsu [5] developed an optimal threshold selection method based on the maximization of the separability of the resultant classes. Thus, due to its simplicity and efficiency Otsu's method was used as threshold estimator in this segmentation algorithm.

The process of threshold selection presented is iteratively used to automatically generate threshold values for multiscale segmentation. For such automatic process, the following algorithm was implemented:

Step 1: Compute the histogram.

Step 2: Compute the optimal threshold.

Step 3: Compute a new histogram for the image with gray levels greater than the threshold.

Step 4: Go to step 2

After perform several tests, it was observed that two iterations of the above algorithm were sufficient to obtain an approximate segmentation of the regions of calcification that will be considered region of interest (ROI).

B. Identification of Calcification from the ROIs

Together with the intensity, another characteristic of the calcification regions is that they are usually followed be an acoustic shadow due to the strong reflection of the ultrasound bean in these regions.

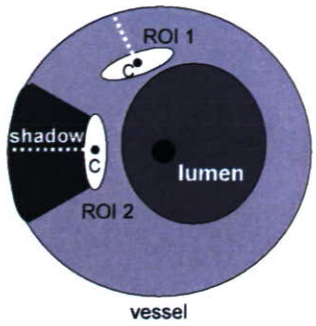

Fig.5 – Example of identification of calcification acoustic shadow .

Thus an efficient way to decide whether a given ROI is a calcification region or not is through analysis of the region posterior to this ROI. As shown in Fig.5.

We can observe in Fig.5 that the region of calcification (ROI 2) is followed by an acoustic shadow and then will present a level for median of the gray level values (in the dotted line) lower then the one of ROI 1.

Thus, in order to detect the acoustic shadow and then determine whether a given ROI is calcification or not, the following algorithm was constructed:

Step 1: Determine the centroid *C* of the ROI.

Step 2: From the centroid of the ROI to the outer boundary of the image, calculate the median gray level value *Med*.

Step 3: If $Med \leq T_{med}$ than classify the ROI as calcification. Else, classify ROI as non-calcification

T_{med} was chosen based on tests with several images.

V RESULT AND DISCUSSIONS II

Using the algorithms for adaptive thresholding and acoustic shadow detection tests were done. Varying the threshold T_{med} in the range from 80 to 210 and observing the number of true positive and false positive, a receiver operating characteristic (ROC) curve was constructed. It is shown in Fig.6. The area under the curve (AUC) is equal to 0.87. For the chosen T_{med}=130 the rate of true positive was 84% and the rate false positive was 12%. Thus, we had sensitivity = 0.84 and specificity = 0.88.

VI CONCLUSIONS

Otsu's algorithm for threshold selection has been successfully applied for segmentation of calcification regions

in IVUS images. However, some bright regions of normal tissue are also, often, segmented. Then an algorithm for identification of the ROIs that are really regions of calcification was implemented taking as identification criteria the presence or absence of acoustic shadow. A ROC curve was plotted showing the performance of the proposed algorithm.

A moment based texture feature together with a position feature presented encouraging results in luminal contour detection . As future works we plan to expand the algorithms for detection of vessel contour and other kind of plaques.

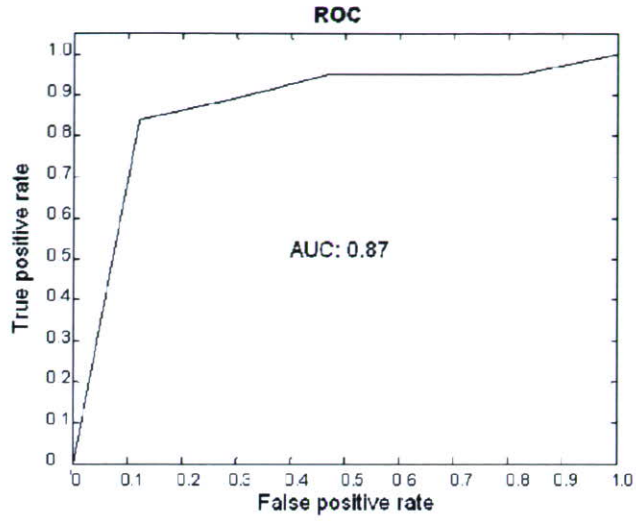

Fig.6 – Receiver Operating Characteristic (ROC) curve.

REFERENCES

[1] E. Brusseau *et al*, Fully automatic luminal contour segmentation in intracoronary ultrasound imaging – a statistical approach, IEEE Trans. on Medical Imaging, Vol. 23, No. 5, pp.554-566, May 2004

[2] E.G.P. Bovenkamp *at al*, Multi-agent segmentation of IVUS images, Pattern Recognition, Elsevier, Vol. 37, pp. 647-663, No. 4, April 2004.

[3] M. Tuceryan, Moment based texture segmentation, Proceedings of 11th IAPR International Conference on Image, Speech, Signal Analysis and Pattern Recognition, pp.45-48, 1992

[4] J.C. Bezdek, Pattern recognition with fuzzy objective function algorithms, Plenum Press, New York, 1981

[5] N. Otsu, A threshold selection method from gray-level histograms, IEEE Trans. on Systems, Man, and Cybernetics, smc-9, pp.62-66, 1979.

Development of Speed-of-Sound Microscopy for Biomedical Applications

Y. Saijo, H. Sasaki, E. Santos Filho, T. Yambe, M. Tanaka
Department of Medical Engineering and Cardiology
Institute of Development, Aging and Cancer, Tohoku University
4-1 Seiryomachi, Aoba-ku, Sendai 980-8575, Japan
saijo@idac.tohoku.ac.jp

N. Hozumi
Department of Electrical and Electronic Engineering
Graduate School, Toyohashi University of Technology
1-1 Tempaku, Toyohashi, 441-8580, Japan

K. Kobayashi, N. Okada
Research & Development Headquarters
Honda Electronics Co. Ltd.
20 Oyamazuka, Oiwa-cho, Toyohashi, 441-3193, Japan

Abstract— **We have been developing a scanning acoustic microscope (SAM) system for medicine and biology featuring quantitative measurement of ultrasonic speed and attenuation of soft tissues. In the present study, we will propose a new concept ultrasonic speed microscopy that can measure the thickness and ultrasonic speed using fast Fourier transform of a single pulsed wave instead of continuous waves used in conventional SAM systems. Six coronary arteries were frozen and sectioned approximately 10 m in thickness. They were mounted on glass slides without cover slips. The scanning time of a frame with 300×300 pixels was 30 s and two-dimensional distribution of ultrasonic speed was obtained. The ultrasonic speed was 1720 m/s in the thickened intima with collagen fiber, 1520 m/s in lipid deposition underlying fibrous cap and 1830m/s in calcified lesion in the intima. These basic measurements will help understanding echogenecity in intravascular ultrasound (IVUS) images. Imaging of coronary artery with the ultrasonic speed microscopy provides important information for study of IVUS coronary imaging.**

Keywords; acoustic microscopy, ultrasonic speed, coronary artery, atherosclerosis

I. INTRODUCTION

Since 1985, we have been developing a scanning acoustic microscope (SAM) system for biomedical use and have been investigating the acoustic properties of various organs and disease states by using this SAM system [1-9]. In biomedicine, SAM is useful for intraoperative pathological examination, study of low-frequency ultrasonic images, and assessment of biomechanics at a microscopic level. The most important feature of our SAM system lies in providing quantitative values of ultrasonic speed and attenuation of thin slices of soft tissue.

In the present study, we will propose a new concept ultrasonic speed microscopy that can measure the thickness and ultrasonic speed using fast Fourier transform of a single pulsed wave instead of continuous waves used in conventional SAM systems. We measured the ultrasonic speed of the tissue components in coronary arteries and the results were compared with IVUS imaging of coronary artery in clinical settings.

II. METHODS

A. Tissue Preparation

Six human coronary artery specimens were involved in the present study. At the autopsy, the coronary arteries were frozen with OCT compounds, sectioned approximately 10 μm in thickness to make a cross-sectional view of coronary artery and mounted on glass slides. The specimens were not stained or not covered with cover slips for ultrasonic speed microscopy observation.

B. Speed-of-Sound Microscopy

Fig. 1 shows a block diagram of speed of sound microscopy for biological tissue characterization. A single ultrasound pulse with a pulse width of 6 ns was emitted and received by the same transducer above the specimen. The aperture diameter of the transducer was 1.2 mm, and the focal length was 1.5 mm. The central frequency was 80 MHz, the bandwidth was 40-150 MHz, and the pulse repetition rate was 10 kHz. The diameter of the focal spot was estimated to be 20 μm at 80 MHz by taking into account the focal distance and

sectional area of the transducer. Distilled water was used as the coupling medium between the transducer and the specimen. The reflections from the tissue surface and those from the interface between the tissue and glass were received by the transducer and were introduced into a Windows-based PC (Pentium 4, 2.8 GHz, 1GB RAM, 80GB HDD) via an analogue-digital converter (Acqiris DP-210, Switzerland). The frequency range was 500 MHz, and the sampling rate was 2 GS/s. Eight values of the time taken for a pulse response at the same point were averaged in order to reduce random noise.

The transducer was mounted on an X-Y stage with a microcomputer board that was driven by the PC through RS232C. The Both X-scan and Y-scan were driven by linear servo motors. Finally, two-dimensional distributions of ultrasonic intensity, speed of sound, attenuation coefficient and thickness of a specimen measuring 2.4×2.4 mm were visualized using 300×300 pixels. The total scanning time was 90 s.

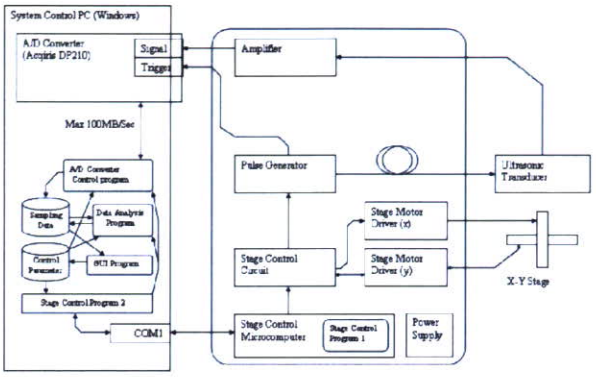

Figure 1. Block diagram of ultrasonic speed microscopy developed with collaboration between Tohoku University, Toyohashi University of Technology and Honda Electronics Co. Ltd.

Fig. 2 shows the appearance of the speed-of-sound microscopy. Whole system can be placed on the desktop.

Figure 2. Apperance of ths speed-of-sound microscopy.

C. *Signal Analysis [10]*

The reflected waveforms are shown in Fig. 3. The waveform at the glass surface without the tissue is shown in (a). This signal was used as a reference waveform. The decline of the glass surface was compensated by measuring three different points in the glass area surrounding the tissue. The waveform from the tissue area is shown in (b). Although the waveform contains two reflections at the surface and at the interface of the tissue and glass, the two components cannot be separated in time domain analysis. Thus, frequency domain analysis was performed by analyzing the interference between the two reflections. Intensity and phase spectra were calculated by Fourier transforming the waveform. The spectra were normalized by the reference waveform. Fig. 4 shows the frequency domain analysis of the interfered waveform.

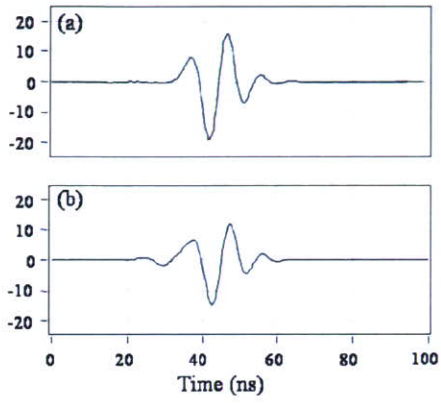

Figure 3. Reflected waveforms (a) from the glass surface without tissue, and (b) from the tissue area

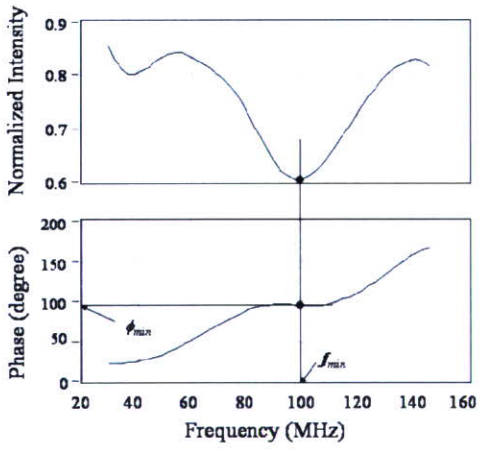

Figure 4. Frequency domain analysis of interfered waveform. ***fmin***: the minimum point in the intensity spectrum, ***φmin***: corresponding phase angle

Denoting the minimum point in the intensity spectrum by f_{min} and the corresponding phase angle by ϕ_{min}, the phase difference between the two reflections at the minimum point is $(2n-1)\pi$, which yields

$$2\pi f_{min} \times \frac{2d}{c_o} = \phi_{min} + (2n-1)\pi \qquad (1)$$

where d, c_0, and n are the tissue thickness, sound speed of water, and a non-negative integer, respectively. Denoting the maximum point in the intensity spectrum by f_{max} and the corresponding phase angle by ϕ_{max}, the phase difference at the maximum point is $2n\pi$, which yields

$$2\pi f_{max} \times \frac{2d}{c_o} = \phi_{max} + 2n\pi \qquad (2)$$

The phase angles ϕ_{min} and ϕ_{max} can be expressed by

$$2\pi f_{min} \times 2d\left(\frac{1}{c_0} - \frac{1}{c}\right) = \phi_{min} \qquad (3)$$

$$2\pi f_{max} \times 2d\left(\frac{1}{c_0} - \frac{1}{c}\right) = \phi_{max} \qquad (4)$$

since ϕ_{min} or ϕ_{max} is the phase difference between the wave that travels the distance $2d$ with sound speed c and the wave that travels a corresponding distance with sound speed c_0. By solving equations (1) and (3),

$$d = \frac{c_0}{4\pi f_{min}}\{\phi_{min} + (2n-1)\pi\} \qquad (5)$$

is obtained for the minimum point. Solving equations (2) and (4) yields

$$d = \frac{c_0}{4\pi f_{max}}(\phi_{max} + 2n\pi) \qquad (6)$$

for the maximum point. Finally, the sound velocity at each frequency is calculated as

$$c = \left(\frac{1}{c_0} - \frac{\phi_{min}}{4\pi f_{min} d}\right) \qquad (7)$$

$$c = \left(\frac{1}{c_0} - \frac{\phi_{max}}{4\pi f_{max} d}\right) \qquad (8)$$

After determination of the thickness, attenuation of ultrasound was then calculated by dividing amplitude by the thickness.

III. RESULTS

Fig. 5 shows a PC window of our speed-of-sound microscopy. The upper left is an amplitude image, the upper right is an ultrasonic speed image, the lower left is an attenuation image and the lower right is the thickness distribution of the normal coronary artery. The intima is thin and speed of sound is 1600 m/s in the intima, 1560 m/s in the media and 1590 m/s in the adventitia, respectively.

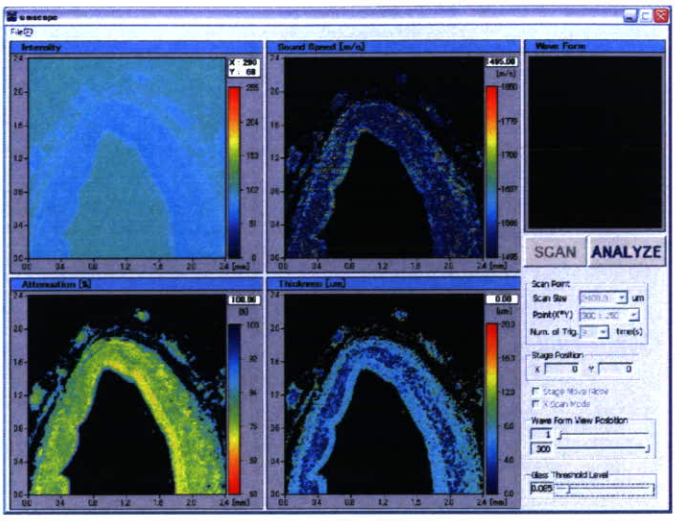

Figure 5. PC window of speed of sound microscopy showing a normal coronary artery. Upper left: amplitude image, upper right: speed of sound image, lower left: attenuation image and lower right: thickness

Fig. 6 is an atherosclerotic coronary artery. The speed of sound is 1680 m/s in the thickened intima with collagen fiber, 1520 m/s in lipid deposition underlying fibrous cap and 1810m/s in calcified lesion in the intima.

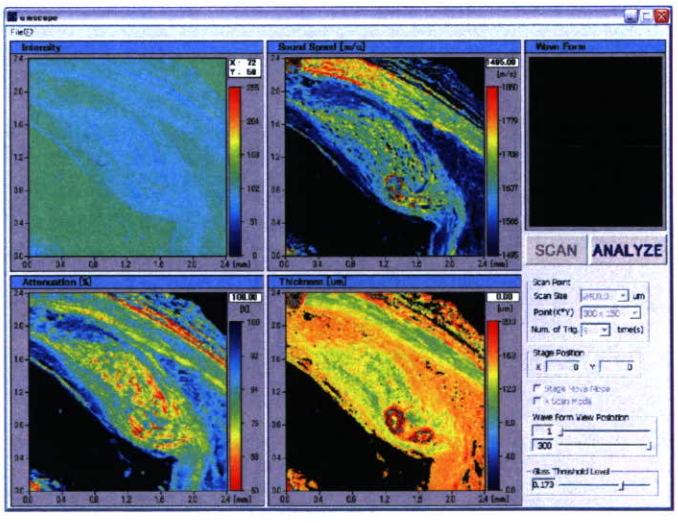

Figure 6. PC window of speed of sound microscopy showing an atherosclerotic coronary artery. Upper left: amplitude image, upper right: speed of sound image, lower left: attenuation image and lower right: thickness.

IV. DISCUSSION

In the present study, speed of sound in the excised human coronary arteries was measured with the ultrasonic speed microscopy. The results would become basic data base for interpretation of clinical IVUS images and novel IVUS imaging technologies.

The results showed that the speed of sound in the intima and adventitia, mainly consisted of collagen fiber, had higher values than those of media, mainly consisted of vascular smooth muscle. The different of acoustic properties may lead to the classical three-layered appearance of normal coronary artery in clinical IVUS imaging. The findings indicate that the echo intensity is not determined by the difference of acoustic impedance between neighboring layers. The distribution and the structure of materials with different acoustic properties may also contribute to the echo pattern in IVUS.

The plaque with a thick fibrous cap consisted of collagen fiber, considered showed higher value of speed of sound than those of normal media. Generally, absorption and scattering are the two main factors of attenuation of ultrasound. Thus, the high scattering within the thickened intima may lead to the high intensity echo in the "hard plaque". Lipid showed speed of sound. These values explain the low echo in the "soft plaque" in the same manner of renal cysts containing water like fluid. Besides its absolute low values, the homogeneity of acoustic properties within the lipid pool may contribute to the low scattering and consequently a lipid pool shows low intensity echo.

V. CONCLUSIONS

We have developed a novel acoustic microscope system that can measure the speed of sound of thin slices of biological material. The most important feature was use of a single pulse and the Fourier transform to calculate the sound speed at all measuring points. Although the data acquisition time of a frame was greater than that in conventional SAM, the total time required for calculation was significantly shorter. The acoustic microscope system can be applied to intraoperative pathological examination.

ACKNOWLEDGMENTS

This study was supported by Grants-in-Aid for Scientific Research (Scientific Research (B) 15300178, Scientific Research (B) 15360217) from the Japan Society for the Promotion of Science and Health and Labor Sciences Research Grants from the Ministry of Health, Labor and Welfare for the Research on Advanced Medical Technology (H17-Nano-001).

REFERENCES

[1] Y. Saijo, M. Tanaka, H. Okawai, F. Dunn, The ultrasonic properties of gastric cancer tissues obtained with a scanning acoustic microscope system, Ultrasound Med Biol 17 (1991), pp. 709-714.

[2] H. Sasaki, M. Tanaka, Y. Saijo, H. Okawai, Y. Terasawa, S. Nitta, K. Suzuki, Ultrasonic tissue characterization of renal cell carcinoma tissue, Nephron 74 (1996), pp. 125-130.

[3] Y. Saijo, M. Tanaka, H. Okawai, H. Sasaki, S. Nitta, F. Dunn, Ultrasonic tissue characterization of infarcted myocardium by scanning acoustic microscopy, Ultrasound Med Biol 23 (1997), pp. 77-85.

[4] Y. Saijo, H. Sasaki, H. Okawai, S. Nitta, M. Tanaka, Acoustic properties of atherosclerosis of human aorta obtained with high-frequency ultrasound, Ultrasound Med Biol 24 (1998), pp. 1061-1064.

[5] Y. Saijo, H. Sasaki, M. Sato, S. Nitta, M. Tanaka, Visualization of human umbilical vein endothelial cells by acoustic microscopy, Ultrasonics 38 (2000), pp. 396-399.

[6] Y. Saijo, T. Ohashi, H. Sasaki, M. Sato, C.S. Jorgensen, S. Nitta, Application of scanning acoustic microscopy for assessing stress distribution in atherosclerotic plaque, Ann Biomed Eng 29 (2001), pp. 1048-53.

[7] H. Sasaki, Y. Saijo, M. Tanaka, S. Nitta, Influence of tissue preparation on the acoustic properties of tissue sections at high frequencies, Ultrasound Med Biol 29 (2003), pp. 1367-72.

[8] Y. Saijo, T. Miyakawa, H. Sasaki, M. Tanaka, S. Nitta, Acoustic properties of aortic aneurysm obtained with scanning acoustic microscopy, Ultrasonics 42 (2004), pp. 695-698.

[9] H. Sano, Y. Saijo, S. Kokubun, Material properties of the supraspinatus tendon at its insertion – A measurement with the scanning acoustic microscopy, J. Musculoskeletal Res. 8 (2004), pp. 29-34.

[10] N. Hozumi, R. Yamashita, C.K. Lee, M. Nagao, K. Kobayashi, Y. Saijo, M. Tanaka, N. Tanaka, S. Ohtsuki, Time–frequency analysis for pulse driven ultrasonic microscopy for biological tissue characterization, Ultrasonics 42 (2004), pp. 717-722.

Imaging for Biological Tissue with Acoustic Impedance Microscope

A.Kimura,S. Terauchi Y.Murakami,
N.Hozumi, M.Nagao, S.Yoshida
Toyohashi University of Technology
Toyohashi, Japan
kimura@boss.eee.tut.ac.jp

K.Kobayashi
Honda Electronics Co.,Ltd
Toyohashi, Japan

Y.Saijo
Tohoku University
Sendai, Japan

***Abstract*—We have proposed a new method for two-dimension for two-dimensional acoustic impedance imaging for biological tissue that can perform micro-scale observation without preparing a sliced specimen. A tissue was attached on a substrate of 0.5mm in thickness. An acoustic pulse was transmitted from the "rear side" of the substrate. The reflection intensity was interpreted into local acoustic impedance of the target tissue. Quantification of acoustic impedance was performed using water or an appropriate material as a reference. As for an observation, rat cerebellum was employed. The development of parallel fiber in cerebella cultures was clearly observed as the contrast in acoustic impedance. The proposed technique is believed to be a powerful tool for biological tissue characterization.**

Keywords-component; biological tissue;acoustic impedance; micro-scale imaging

I. INTRODUCTION

In most of optical observation of biological tissue, the specimen is sliced into several micrometers in thickness, and fixed on a glass substrate. The microscopy is obtained by transmitted light through the specimen. As it is normally not easy to get a good contrast by local difference in refraction and/or transmission spectrum, the specimen is usually stained before being observed. However the staining has some disadvantages. It normally takes from several hours to several days to finish the process. Furthermore, the tissue, after being stained, often completely loses its biological functions; i.e., the observation with staining process is chemically destructive.

The authors previously proposed a pulse driven ultrasonic sound speed microscopy that can obtain sound speed image in a short time[1-2]. Although a small roughness of the specimen was approved in this type of microscope, slicing the specimen into several micrometers was still required for the observation.

Based on the above background, the authors newly propose the acoustic impedance microscopy that can image the local distribution of cross sectional acoustic impedance of tissue. As acoustic impedance is given as a product of sound speed and density, it would have a good correlation with sound speed, when the variance in density was not significant

II. EXPERIMENTAL SETUP

Fig. 1 illustrates the outline of the acoustic impedance microscope. Distilled water was used for the coupling medium between the substrate and transducer. A sharp electric pulse of about 40 V in peak voltage and 2 ns in width was generated by the pulse generator. The maximum repetition rate of the pulse was as high as 10 kHz. The transducer was PVDF-TrFE type of which focal length was 3.0 mm. An acoustic wave with a wide frequency component was generated by applying the voltage pulse. The acoustic wave, being focused on the interface between the substrate and tissue, was transmitted and received by the same transducer. Two-dimensional profile of acoustic impedance was obtained by mechanically scanning the transducer using the stage driver, keeping the focal point on the rear surface of the substrate.

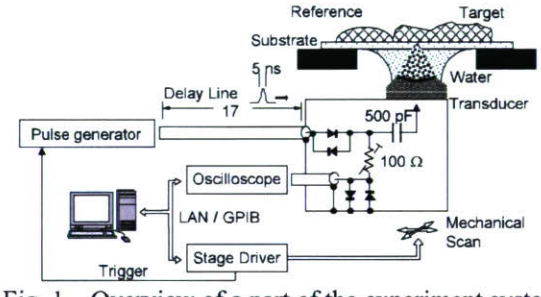

Fig. 1 Overview of a part of the experiment system.

III. CALIBERATION

Figure 2 illustrates the calibration of acoustic impedance. The target signal is compared with the reference signal. Hereafter, the signal component at an arbitrary frequency will be symbolized by S. Considering the reflection coefficient, the target signal S_{target} can be described as

$$S_{target} = \frac{Z_{target} - Z_{sub}}{Z_{target} + Z_{sub}} S_0$$

where S_0 is the transmitted signal, Z_{target} and Z_{sub} are the acoustic impedances of the target and substrate, respectively. On the other hand, the reference signal can be described as

$$S_{ref} = \frac{Z_{ref} - Z_{sub}}{Z_{ref} + Z_{sub}} S_0$$

where Zref is the acoustic impedance of the reference material. We can measure Starget and Zref, however, S0 can not be directly measured. The acoustic impedance of the target is

subsequently calculated as a solution of the simultaneous equations for Z_{target} and S_0, as

$$Z_{target} = \frac{1-\frac{S_{target}}{S_0}}{1+\frac{S_{target}}{S_0}} Z_{sub} = \frac{1-\frac{S_{target}}{S_{ref}} \cdot \frac{Z_{sub}-Z_{ref}}{Z_{sub}+Z_{ref}}}{1+\frac{S_{target}}{S_{ref}} \cdot \frac{Z_{sub}-Z_{ref}}{Z_{sub}+Z_{ref}}} Z_{sub}$$

assuming that S_0 is constant throughout the observation process.

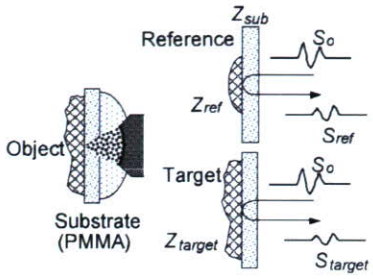

Fig.2 Illustration for calibration of the acoustic impedance.

IV. OBSERVATION OF CEREBELLAR CORTEX OF A RAT

Figure. 3 shows the observed images of cerebellar cortex of a rat at immature (P1; postnatal 1 day), transient (P7), and mature (P20) stages. All the specimens in Fig. 3 had been chemically fixed.

In the immature cerebellar cortex (P1), the external granular layer (EGL), the outer layer of the cortex, showed higher impedance compared to the inner layer. The area indicated by the rectangle in the acoustic image is morphologically corresponding to the immunohistochemical observation, although the scale is not completely corresponded because the tissue was somehow subjected to compression during the acoustic observation. At this stage, as myelin is not yet generated, the existence of white matter (WM) is not clearly observed.

In the medium stage, four different layers; the WM, internal granular layer (IGL), Purkinje layer (PL) and EGL become to be comprehensive. The EGL and IGL showed higher impedance than the PL and WM. Morphological correspondence between acoustic and immunohistological observation is however not clear in these images.

In the mature stage, the EGL, which is composed of small neuronal cell bodies, has developed into the molecular layer (ML), which is composed of elongated axon (neurite), called parallel fibers. The four layers, WM, IGL, PL and ML are more clearly observed in acoustic image. The correspondence with immunohistological observation is also clearly seen.

It should be noted that very similar image were observed by simply contacting a cross section of the whole tissue with the substrate, without performing chemical fixation.

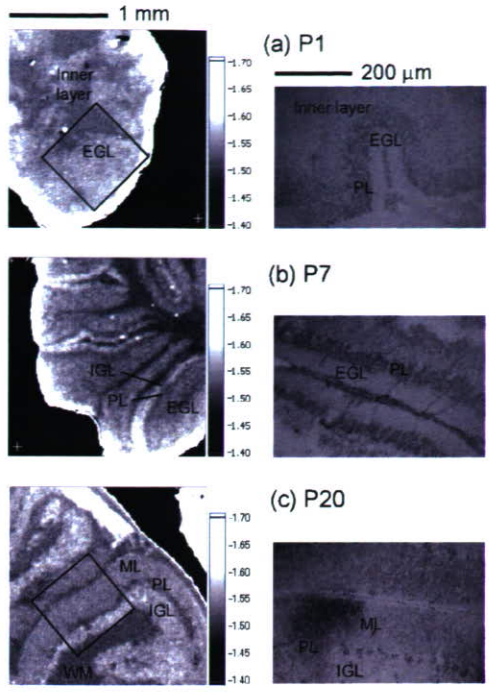

Fig.3Two-dimensional profiles of acoustic impedance ($x10^6 Ns/m^3$) of cerebellar cortex (left) and optical microcopies(right).Specimen:rat, sagittal cross section, chemically fixed.

V. DISCUSSION

Considering the precision of the calibration, the reference material should be stable in both physical and chemical properties, and should strongly adhere to the substrate. It is recommended that the acoustic impedance of the reference is close to that of the target. Furthermore, as for the substrate, most of available materials have higher acoustic impedance than biological tissues. In such cases, the phase of the transmitted signal is reversed at the interface. The acoustic impedance of the substrate should be sufficiently high compared to that of the target, in order to retain a strong reflection. However extremely high acoustic impedance of the substrate may increase the reflection coefficient at the interface between the coupling medium and substrate, and reduce the intensity of transmitted signal to the target. This would obviously reduce the S/N ratio. Therefore, in order to obtain a good S/N ratio, the materials should be carefully selected considering their accordance.

REFERENCES

[1] N. Hozumi, R. Yamashita, C-K Lee, M. Nagao, K. Kobayashi, Y. Saijo, M. Tanaka, N. Tanaka & S Ohtsuki: "Ultrasonic Sound Speed Microscope for Biological Tissue Characterization Driven by Nanosecond Pulse", *Acoustic Science & Technology*, 20, 386 (2003).

[2] N. Hozumi, R. Yamashita, C-K. Lee, M. Nagao, K. Kobayashi, Y. Saijo, M. Tanaka, N. Tanaka & S.Ohtsuki: "Time –frequency analysis for pulse driven ultrasonic microscopy for biological tissue characterization", *Ultrasonics*, 42, 717 (2003).

Increased Sound Speed of Synovial Membrane after Immobilization Assessed by Scanning Acoustic Microscopy

Yoshihiro Hagiwara1*, Yoshifumi Saijo2, Fujio Matsumoto1, Eiichi Chimoto1, Yasuyuki Sasano3, Shoichi Kokubun1

1Department of Orthopaedic Surgery, Tohoku University Graduate School of Medicine, 2Department of Medical Engineering and Cardiology, Institute of Development, Aging and Cancer, Tohoku University, 3Division of Craniofacial Development and Regeneration, Tohoku University Graduate School of Dentistry

Sendai, Japan

hagi@mail.tains.tohoku.ac.jp

Abstract

Objectives: The biomechanics of immobilized joints is not well understood. The present study was designed to investigate the tissue elasticity of the anterior and posterior synovial membrane (SM) in a rat immobilized knee model using scanning acoustic microscopy (SAM).

Methods: Thirty rats had their knee joints immobilized with a plate and metal screws. The rats were fixed at 1, 2, 4, 8 and 16 weeks after surgery and the knee joints were sectioned sagittally. A new concept SAM using a single pulsed wave instead of continuous waves was applied to measure the sound speed of the anterior and posterior SM, comparing it with the corresponding light microscopic images.

Results: The sound speed of the posterior SM increased significantly in the 8- and 16-week experimental group compared with that in the control group. The sound speed of the anterior SM showed no statistical difference between the experimental and the control groups at any period of immobilization.

Conclusions: Our data suggest that the increased elasticity of the posterior SM after a long period of immobilization in flexion is one of the main causes of limited extension. SAM is a powerful tool for evaluating the elasticity of targeted tissues.

Keywords-immobilization, knee, contracture, scanning acoustic microscopy, elasticity, synovial membrane

I. INTRODUCTION

Joint contracture is defined as a decrease in both active and passive ranges of motion (ROM) after immobilization. The decreased ROM limits the activity of daily living in various aspects. Immobilization, which is a major cause of joint contracture, is beneficial for decreasing pain caused by trauma and preventing the joint from damage in the acute phase of arthritis such as pyogenic and rheumatoid arthritis (1-3). Even by extensive rehabilitation or surgical treatment, however, it is difficult to regain the full ROM in an established joint contracture after a long period of immobilization (4,5).

The components of joint contracture after immobilization are classified into arthrogenic and myogenic ones. The arthrogenic components are lesions of bone, ligaments, capsule and synovial membrane (SM), while the myogenic components are lesions of muscle, tendon and fascia (6,7). Some investigators have attributed contracture to myogenic causes (8), while others attributed it to arthrogenic causes (4,7,9-13). It is difficult to evaluate such contradictory reports because different animal species and methods were used in their immobilization experiments. Among the arthrogenic components, the stiffness of the capsule and SM through synovial atrophy, retraction, fibrosis, and adhesion may contribute to the limited ROM (1,7,8,10,14-17). Though increased elasticity of the capsule or SM has been suggested to be a cause of joint contracture (18), it is not known yet how the elasticity is affected by immobilization.

A conventional scanning acoustic microscopy (SAM) using continuous waves characterizes biological tissues by determining the elastic parameters based on the sound speed (19). Recent studies on infarcted myocardium (20), atherosclerosis of aorta (21) and carotid arterial plaques (22) have shown that the acoustic properties reflect the collagen types. Though this traditional system still works today, it is not practical because it takes much time to analyze the data.

In the present study, we applied a new concept SAM using single pulsed wave, which can make total time for calculation significantly shorter, to examine the elasticity of the anterior and posterior SM (synovial intima and subintima) in the course of knee joint immobilization in a rat experimental model.

II. MATERIALS AND METHODS

Animals

The protocol for this experiment was approved by the Animal Research Committee of Tohoku University. Adult male Sprague-Dawley rats weighing from 380 to 400 g were used. Their knee joints were immobilized at 145° in flexion with a plastic plate and metal screws for various periods (1, 2, 4, 8 and 16 weeks) (3). The knee joint capsule and the joint itself were untouched (Figure 1A). Sham operated animals had holes drilled in the femur and tibia and screws inserted but none of them were plated. The immobilized animals and the

sham operated animals made up the experimental groups and the control groups, respectively (n=3/ each group).

Tissue Preparation

The rats were fixed with 4% paraformaldehyde in 0.1M phosphate-buffer by perfusion through the aorta. The knee joints were resected and kept in the same fixative. The fixed specimens were decalcified in 10% EDTA in 0.01M phosphate-buffer. The embedded tissue was cut into 5-μm thick sagittal sections from the medial to the lateral side of the joint. Standardized serial sections of the medial midcondylar region of the knee were made. The serial sections were prepared for hematoxylin-eosin to observe the histological appearance of SM after immobilization.

Scanning acoustic microscopy

Our SAM consists of five parts: 1) ultrasonic transducer, 2) pulse generator, 3) digital oscilloscope with PC, 4) microcomputer board and 5) display unit (Figure 2). A single pulsed ultrasound with 5 ns pulse width was emitted and received by the same transducer above the specimen. The aperture diameter of the transducer was 1.2 mm and the focal length was 1.5 mm. The central frequency was 80 MHz and the pulse repetition rate was 10 kHz. Considering the focal distance and the sectional area of the transducer, the diameter of the focal spot was estimated as 20 μm at 80 MHz. Distilled water was used as the coupling medium between the transducer and the specimen. The reflections from the tissue surface and from interface between the tissue and the glass were received by the transducer and were introduced into a digital oscilloscope (Tektronics TDS 5052, USA). The frequency range was 300 MHz and the sampling rate was 2.5 GS/s. Four pulse responses at the same point were averaged in the oscilloscope in order to reduce random noise.

The transducer was mounted on an X-Y stage with a microcomputer board that was driven by the computer installed in the digital oscilloscope through an RS-232C. The X-scan was driven by a linear servo-motor and the Y-scan was driven by a stepping motor. Finally, two-dimensional distributions of the ultrasonic intensity, sound speed and thickness of the 2.4 by 2.4 mm specimen area were visualized with 300 by 300 pixels. The total scanning time was 121 sec.

Signal Analysis

The reflected waveform comprises two reflections at the surface and the interface between the tissue and the glass. The thickness and sound speed were calculated by Fourier-transforming the waveform (19).

Image analysis

Normal light microscopic images corresponding to the stored acoustic images were captured (DMLB 100 HC light microscope, LEICA Wetzlar, Germany). A region of analysis by SAM was set in the anterior and posterior SM each in each section (Figure 1B). In the region, the sound speed of SM, excluding meniscus, bone and cartilage, was calculated with a gray scale SAM images using commercially available image analysis software (PhotoShop 6.0, Adobe Systems Inc., San Jose, CA). SAM images with a gradation color scale were also produced for clear visualization of the sound speed. The optical and acoustic images were compared to ensure morphological congruence in the analysis.

Statistics

All data were expressed as the mean ± SD. The statistical significance of difference in the results was evaluated by unpaired analysis of variance, and *P* values were calculated by Tukey's method. A *P* value less than 0.05 was considered statistically significant.

III. RESULTS

The gradation color images of the posterior SM in the experimental group differed from that in the control group (Figure 3). The posterior SM was composed of low sound speed area (black to blue) in 2-week immobilization (Figure 3A). Low sound speed area was decreased and high sound speed area (yellow to red) gradually increased in the posterior SM of the experimental group with time (Figure 3B). The posterior SM was remained same in all the control groups (Figure 3C).

The anterior SM was similar in all the experimental and control groups irrespective of immobilization periods (data not shown).

The sound speed of the posterior SM is shown in Figure 4. There was no statistical difference between the experimental and the control groups in 1-, 2- or 4-week immobilization. In 8- and 16-week immobilization, however, the sound speed in the experimental group was significantly higher than that in the control group (8w: 1565 m/s±7.61 m/s vs 1639 m/s±6.02 m/s; $p<0.005$, 16w: 1551 m/s±12.5 m/s vs 1650 m/s±9.18 m/s; $p<0.005$) (Figure 4A). There was no statistical difference in the anterior SM in all the experimental and the control groups at any period of immobilization (Figure 4B).

IV. DISCUSSION

The arthrogenic component has been considered as an important factor of joint contracture after immobilization (1,7,8,10,14-18). In a study using a rabbit knee contracture model, the biomechanical characteristics were quantified by a torque-angular displacement diagram (18). The knees in 9-week immobilization in flexion showed a significantly larger torque in extension in the experimental groups than in the control groups even after total extra-articular myotomies. In the same rat model as ours in the present study but immobilized up to 32-week, ROM in extension remained still restricted even after total extra-articular myotomies, which suggested the myogenic restriction proportionally decreased over time (7). In canine glenohumeral joint immobilized up to 16 weeks, the intra-articular pressure rose higher by injection of Hypaque contrast medium and the filling volume was smaller comparing with the control group at a rupture of the capsule (23). These studies suggest that among the arthogenic components, the capsule and SM may most contribute to making joint contracture.

Previous studies analyzed the elasticity of the joint as a whole with or without muscles including ligament, capsule and SM (7,15,18,23). But it was impossible to evaluate the elasticity of the individual arthrogenic components, especially

of capsule and SM in those studies. The present study is the first that measured the elasticity of SM in situ by SAM in rat immobilized knees and revealed the increased elasticity of SM as one of the main causes of joint contracture.

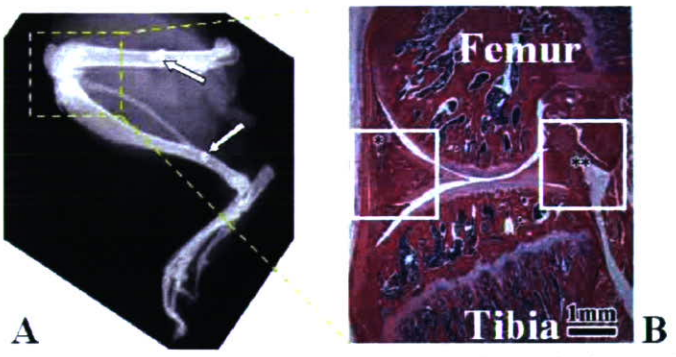

Figure 1: Method of joint immobilization and micorphotograph of a sagittal section in the medial midcondylar region of a rat knee. .
A, Lateral radiograph of the experimental group with a radiolucent plate (20v, 2.0mA, 10sec). Arrows indicate metal screws. **B**, Squares indicate the region of analysis by scanning acoustic microscopy in the anterior (＊) and posterior (＊＊) synovial membrane. (Original magnification × 10, hematoxylin-eosin stain)

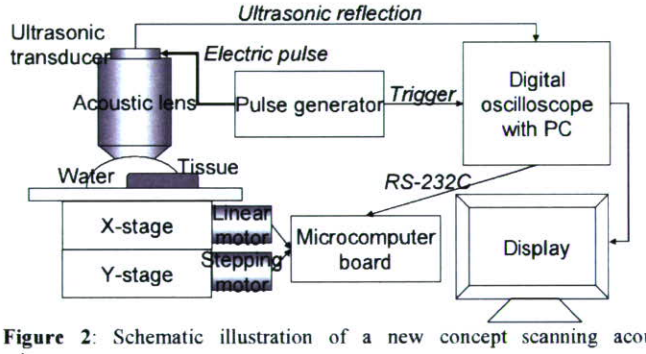

Figure 2: Schematic illustration of a new concept scanning acoustic microscopy.

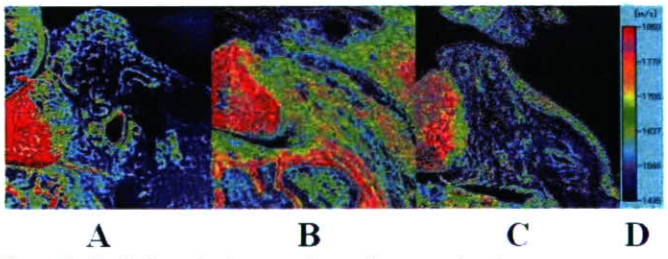

Figure 3: Gradation color images of scanning acoustic microscopy.
A, 2-week immobilization group. **B**, 16-week. **C**, a representative of the control groups (16-week). **D**, gradation color table.

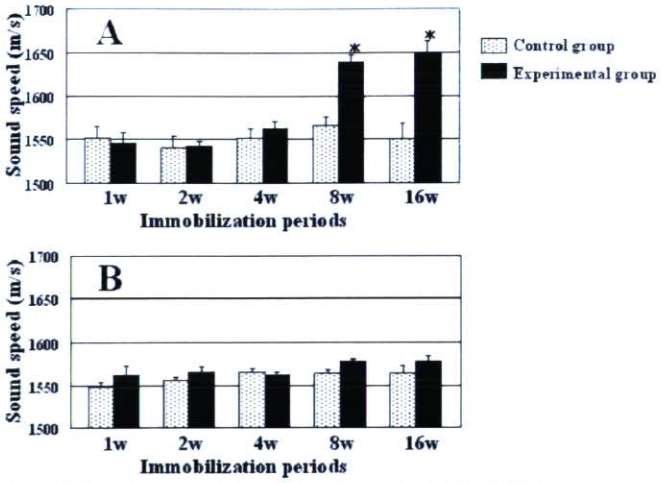

Figure 4: Sound speed changes of the synovial membrane (SM).
A, the posterior SM. **B**, the anterior SM. In the posterior SM, significant difference of sound speed is seen in 8- and 16-week immobilization. There was no statistical difference at any period of immobilization in the anterior SM. * = $P < 0.005$.

Acknowledgment

The authors would like to acknowledge their valued input and efforts of Mr. Katsuyoshi Shoji, Mrs. Michiko Fukuyama and Miss Haruka Sasaki and thank Dr. Hans K Uhtoff and Dr. Guy Trudel for their technical advice of making the animal model.

References

[1] Trudel G, Seki M, Uhthoff HK. Synovial adhesions are more important than pannus proliferation in the pathogenesis of knee joint contracture after immobilization: an experimental investigation in the rat. J Rheumatol, vol27, pp. 351-357, 2000.

[2] Patridge REH, Duthie JJR. Controlled trial of the effect of complete immobilization of the joints in rheumatoid arthritis. Ann Rheum Dis, vol 22, pp.91-99, 1963.

[3] Gault SJ, Spyker JM. Beneficial effect of immobilization of joints in rheumatoid and related arthritis: A splint study using sequential analysis. Arthritis Rheum, vol 12, pp. 34-44, 1969.

[4] Peacock EE. Some biochemical and biophysical aspects of joint stiffness: role of collagen synthesis as opposed to altered molecular bonding. Ann Surg, vol 64, pp.1-12, 1966.

[5] Damron TA, Greenwald TA, Breed A. Chronological outcome of surgical tendoachilles lengthing and natural history of gastro-soleus contracture in cerebral palsy. Clin Orthop, vol 301, pp. 249-255, 1994.

[6] Trudel G.. Differentiating the myogenic and arthrogenic components of joint contractures. An experimental study on the rat knee joint. Int J Rehabil Res,vol 20, pp. 397-404, 1997.

[7] Trudel G, Uhtoff HK. Contractures secondary to immobility: is the restriction articular or muscular? An experimental longitudinal study in the rat knee. Arch Phys Med Rehabil, vol 81, pp. 6-13, 2000.

[8] Evans BE, Eggers GWN, Butler JK, Blumel J. Experimental immobilization and remobilization of rat knee joints. J Bone Joint Surg, vol 42A, pp. 737-758 1960.

[9] Amiel D, Akeson WH, Harwood FL, Mechanic GL. The effect of immobilization on the types of collagen synthesized in periarticular connective tissue. Connect Tissue Res, vol 8, pp. 27-32, 1980.

[10] Enneking WF, Horowits M. The Intra-articular effects of immobilization on the human knee. J Bone Joint Surg, vol 54A, pp. 973-985, 1972.

[11] Hall MC. Cartilage changes after experimental immobilization of the knee joint of the young rat. J Bone Joint Surg, vol 45A, pp. 35-44, 1963.

[12] Wilson PD. Capsulectomy for the relief of flexion contractures of the elbow following fracture. J Bone Joint Surg, vol 26A, pp. 71-86, 1944.

[13] Wagner LC. Fixed extension of the knee due to capsular contraction. NY State J Med, vol 48, pp. 194-198, 1948.

[14] Trudel G, Desaulniers N, Uhthoff HK, Laneuville O. Different levels of COX-1 and COX-2 enzymes in synoviocytes and chondrocytes during joint contracture formation. J Rheumatol, vol 28, pp. 2066-2974, 2001.

[15] Trudel G, Uhthoff HK, Brown M. Extent and direction of joint motion limitation after prolonged immobility: an experimental study in the rat. Arch Phys Med Rehabil , vol 80, pp. 1542-1547, 1999.

[16] Finsterbush A, Friedman B. Early changes in immobilized rabbit knee joints: a light and electron microscopic study. Clin Orthop, vol 92, pp. 305-319, 1973.

[17] Roy S. Ultrastructure of articular cartilage in experimental immobilization. Ann Rheum Dis, vol 29, pp. 634-642, 1970.

[18] Woo SL, Matthews JV, Akenson WH, Amiel D, Convery FR. Connective tissue response to immobility: Correlative study of biomechanical measurements of normal and immobilized rabbit knees. Arthritis Rheum,vol 18, pp. 257-264, 1975.

[19] Hozumi N, Yamashita R, Lee CK, Nagao M , Kobayashi K, Saijo Y, Tanaka M, Tanaka N, Ohtsuki S. Time-frequency analysis driven ultrasonic microscopy for biological tissue characterization. Ultrasonics, vol 42, pp. 717-722, 2004.

[20] Saijo Y, Tanaka M, Okawai H, Sasaki H, Nitta S, Dunn F. Ultrasonic tissue characterization of infracted myocardium by scanning acoustic microscopy. Ultrasoud Med Biol, vol 23, pp. 77-85, 1997.

[21] Saijo Y, Sasaki H, Okawai H, Nitta S, Tanaka M. Acoustic properties of atherosclerosis of human aorta obtained with high-frequency ultrasound. Ultrasound Med Biol, vol 24, pp. 1061-1064, 1998.

[22] Saijo Y, Jorgensen S, Mondek P, Sefranek V, Paaske W. Acoustic inhomogeneity of carotid arterial plaques determined by GHz frequency range microscopy. Ultrasound Med Biol, vol 28, pp. 933-977, 2002.

[23] Shollmeier G, Sarkar K, Fukuhara K, Uhtoff HK. Structural and functional changes in the canine shoulder after cessation of immobilization. Clin Orthop, vol 323, pp. 310-315, 1996.

The High-frequency Acoustic Properties of the Rabbit Supraspinatus Tendon Insertion

A comparison between decalcified and undecalcified specimens

Hirotaka Sano, MD†, Koshi Hattori, MD†, Yoshifumi Saijo, MD‡
and Shoichi Kokubun, MD†
†Department of Orthopaedic Surgery, Tohoku University, School of Medicine
‡Department of Medical Engineering and Cardiology, Institute of Development, Aging and Cancer, Tohoku University
Sendai, Japan
E-mail: staka@mail.tains.tohoku.ac.jp

Abstract— To clarify whether decalcification altered the tissue high-frequency acoustic properties or not, supraspinatus tendon insertion of 6 Japanese white rabbits were measured with scanning acoustic microscopy. Right supraspinatus tendons attached to the humeral head were cut into two pieces at the center of the tendon. Then, they were fixed with 10% neutralized formalin for 12 hours. In each specimen, medial half was not decalcified, while lateral half was decalcified with ethylene-diamine-tetra-acetic acid. After embedding in paraffin, they were cut at a thickness of 5μm for the measurement with scanning acoustic microscopy. The sound speed in each histologic zone was evaluated, which were then compared between the undecalcified and the decalcified specimens.

Mean sound speed of non-mineralized fibrocartilage was 1575m/s in the undecalcified specimens and 1572m/s in the decalcified specimens. On the other hand, it decreased 3-5% after decalcification in the mineralized tissue including mineralized fibrocartilage and bone (mineralized fibrocartilage: undecalcified = 1756m/s, decalcified = 1672m/s; bone: undecalcified = 1800m/s, decalcified = 1746m/s). However, no statistically significant differences were found between the undecalcified and the decalcified specimens. We believe that the scanning acoustic microscopy can be applied for the specimens including mineralized tissue after decalcification.

Keywords-Scanning acoustic microscopy, sound speed, supraspinatus tendon, insertion, decalcification

I. INTRODUCTION

Scanning acoustic microscopy (SAM) has been used to assess the high-frequency acoustic properties of various types of soft tissue, representing complex histologic structures, i.e. cardiac muscles, arterial plaques and vascular walls, etc **[1-3]**. One of the major advantages of SAM is that tissue elasticity can be measured with formalin-fixed and paraffin-embedded glass slides. This makes it possible to compare the 2-dimensional distribution of the tissue elasticity to the histologic structure. Since, however, the role of decalcification has not been investigated yet in SAM measurement, we attempted to clarify the roles of decalcification in SAM measurement in the current study. Especially, we hoped to know whether decalcification alter the tissue high-frequency acoustic properties of the non-mineralized fibrocartilage at the insertion of the rabbit supraspinatus tendon or not.

II. MATERIALS AND METHODS

A. Preparation of the specimens

Supraspinatus tendon insertions of 6 Japanese white rabbits were used for the current study. All these animals were 12 month-old males and their average body weight was 2.3kg (range: 2.2-2.4kg). After euthanasia with overdosed pentobarbital, right supraspinatus tendons attached to the humeral head were collected. The specimens were cut into two pieces at the center of supraspinatus tendon in line with its fibers and bony tissue was carefully removed except for the insertion site. Then, they were fixed with 10% neutralized formalin for 12 hours.

In each animal, medial half of the specimen was not decalcified, while lateral half of the specimen was decalcified with ethylene-diamine-tetra-acetic acid (EDTA). After embedding in paraffin, they were cut at a thickness of 5μm both for the histologic staining and for the measurement with SAM.